https://doi.org/10.5194/egusphere-2024-3580
Preprint. Discussion started: 23 January 2025

A mutlisensor C-band synthetic aperture radar (SAR) approach to retrieve freeze/thaw cycles: A case study for a low Arctic environment

Charlotte Crevier[1,2], Alexandre Langlois[1,2], Chris Derksen[3], Alexandre Roy[2,4]

[1]Centre d'Applications et de Recherches en Télédétection (CARTEL), Université de Sherbrooke, Sherbrooke, J1K 2R1, Canada
[2]Centre d'Études Nordiques, Université Laval, Québec, QC, G1V 0A6, Canada
[3]Environment and Climate Change Canada, Climate Research Division, Toronto, ON, M3H 5T4, Canada
[4]Département des Sciences de l'Environnement, Université du Québec à Trois-Rivières, Trois-Rivières, QC, Canada, G9A 5H7

Correspondence to: Alexandre Roy (Alexandre.Roy@uqtr.ca)

Abstract. This study investigates the spatial variability of surface freeze/thaw (F/T) cycles in low arctic tundra retrieved from multisensor SAR backscatter time series. To increase the temporal resolution of SAR observations, we combined measurements from Sentinel-1 and RADARSAT-2. An incidence angle normalization was applied to the backscatter time series to remove the influence of the acquisition angle on backscatter. A seasonal threshold algorithm (STA) was used to detect F/T transitions and applied to HH, HV and HH+HV polarization datasets. The classification threshold was optimized using soil temperature measurements from spatially distributed sites. A detection accuracy of over 93% was calculated with an optimized classification threshold of 0.62 for the HH+HV time series on those sites. We created surface F/T day of the year (DOY) maps of the study area for the 2018 and 2019 freezing transitions, and for the 2019 thawing transition using the HH+HV time series with the optimized classification threshold. Those maps were combined with a terrestrial ecosystem (ecotype) map to investigate the impact of ecotypes on the F/T transitions. Three generalized least squares (GLS) models were fitted on the coupling of the maps. Differences of about 2–3 days were observed between ecotype classes. Based on these differences, we hypothesize that differences during the freezing transition were probably due to the underlying soil moisture and during the thawing transition, to the influence of vegetation. Our study demonstrates the power of merging two C-band SAR time series to create near-daily F/T maps over arctic environment to allow for better understanding of surface F/T processes happening at small spatial scale in arctic environments.

1 Introduction

Over the last four decades, important signs of climate change have been observed across the Arctic (Dai et al., 2019) amplified by enhanced warming due to positive climate feedback (Serreze and Barry, 2011). The observed increase in surface temperatures at two to three times the rate observed elsewhere on the planet has significant impacts on the cryosphere and arctic ecosystems. Increased air temperature across the Arctic influences several cryosphere-related phenomena, such as the

https://doi.org/10.5194/egusphere-2024-3580
Preprint. Discussion started: 23 January 2025

precipitation type and phase (Il Jeong and Sushama, 2018; Langlois et al., 2017), the snow cover accumulation and distribution (Derksen and Brown, 2012), the spatial and temporal evolution of vegetation cover (Bjorkman et al., 2018; Martin et al., 2017), and the soil thermal regime (Smith et al., 2010), including permafrost temperature and active layer depth.

The permafrost active layer refers to the soil surface layer which undergoes an annual freeze and thaw (F/T) cycle. This cycle impacts the surface energy budget (Schuur et al., 2015), hydrological and carbon cycles (Wang et al., 2009), vegetation growing seasons (Kim et al., 2012), underlying permafrost state and active layer thickness (ALT; Yi et al., 2018). Snow strongly influences those processes because of its low thermal conductivity and its high albedo that regulate ground temperatures (Domine et al., 2019; Zhang et al., 2018). As such, snowpack properties like total depth, density, and microstructure influence the F/T cycles of the underlying soil (Prince et al., 2019). However, one of the most significant consequences of a warming Arctic is a reduction in snow cover duration with the snow cover forming later in the fall and melting early in the spring (Derksen and Brown, 2012; Brown et al., 2017). Furthermore, tundra vegetation, which modulates snow distribution through trapping effects (Barrere et al., 2018; Busseau et al., 2017; Royer et al., 2021), is also changing significantly (Bjorkman et al., 2018; Martin et al., 2017). Royer et al. (2021) suggested that changes in the snowpack microstructure and distribution patterns, linked to the increase of vegetation height and coverage, could further amplify permafrost warming (Callaghan et al., 2011).

Several studies have developed F/T detection algorithms using satellite passive microwave (PMW) measurements (Chen et al., 2019; Derksen et al., 2017; Kim et al., 2011; Prince et al., 2018; Rautiainen et al., 2016; Roy et al., 2015, 2020; Xu et al., 2016; Zheng et al., 2017). The potential of using low-frequency passive microwave data for developing F/T cycle detection algorithms have increased due to the available L-Band satellite missions (e.g., Aquarius, SMOS, SMAP). Despite the clear potential for detecting and monitoring soil F/T cycles, the strong landscape heterogeneity within the coarse grid spacing of these datasets (~25 km) leads to a misrepresentation of the spatial variability, biases, and uncertainty in the F/T retrievals (Ponomarenko et al., 2019; Prince et al., 2019).

Satellite Synthetic Aperture Radar (SAR) measurements fill this gap, because of their much finer spatial resolution: typically, from 1 m to 100 m. The SAR backscatter signal (sigma nought; σ^0) depends on the dielectric (e.g., moisture and water phase) and geometric (e.g., roughness) properties of the target, leading to a strong sensitivity to dielectric contrasts during soil surface phase transition seasons (i.e., freezing and thawing). Given the very high dielectric constant of water in the microwave spectrum, the dielectric constant for dry or frozen soil is small compared to that of wet or thawed soils (Ulaby et al., 1986). SAR backscatter information can thus help to detect changes in the dielectric constant of the soil surface during F/T cycles for different ecosystems (Baghdadi et al., 2018; Chen et al., 2018; Chen et al., 2019; Cohen et al., 2021; Jagdhuber et al., 2014; Park et al., 2011). C-Band SAR observations generally allow to get the signal from the soil top layer with a limited penetration depth of about 5 cm depending on the properties of the soil (Ulaby et al., 1986). The easy access to PMW data and its daily

https://doi.org/10.5194/egusphere-2024-3580
Preprint. Discussion started: 23 January 2025

temporal coverage have favoured their use compared to SAR data in the detection of F/T cycles (Park et al., 2011). However, constellations such as Sentinel-1 (since 2016; Bourbigot et al., 2016) and the RADARSAT Constellation Mission (RCM; since 2019) allow improved temporal coverage of σ^0 data, thus increasing the potential for daily observations across the Arctic.

This study aims to retrieve surface F/T cycle onset in a low arctic tundra environment using SAR backscatter time series. This paper thus aims to (1) create a near-daily multisensor C-band normalized backscatter time series, and (2) evaluate those time series' potential to retrieve surface F/T cycles, using a simple seasonal classification algorithm and a study site in a low arctic environment. This case study relies on a unique ecotype map created from unsupervised classification of 2011 WorldView-2 multispectral imagery (Ponomarenko et al., 2019) based on the Canadian arctic-subarctic Biogeoclimatic Ecosystem Classification (CASBEC) defined in McLennan et al. (2018).

2 Study site and data

2.1 Overview of the study area

This study focuses on the Intensive Monitoring Area (IMA) north of the Greiner Lake watershed, near Cambridge Bay, Victoria Island, NU, Canada (Figure 1). The site is instrumented with a meteorological station and characterized by low and sparse vegetation, low annual precipitation, and flat topography, typical of arctic tundra environments. The IMA region was chosen due to the availability of a unique high-resolution detailed ecotype map (section 2.2.3) which will be used for the small-scale spatial variability case study. The mean annual air temperature is around -10 ºC, and rarely goes above 18 ºC during the warm season or below -41 ºC during the cold season. For our study, we used daily soil temperature data derived from a spatially distributed network of i-Buttons deployed across the IMA over 2018–2019, in the most dominant ecotypes (Ponomarenko et al., 2019) present in the area (Figure 1)

https://doi.org/10.5194/egusphere-2024-3580
Preprint. Discussion started: 23 January 2025

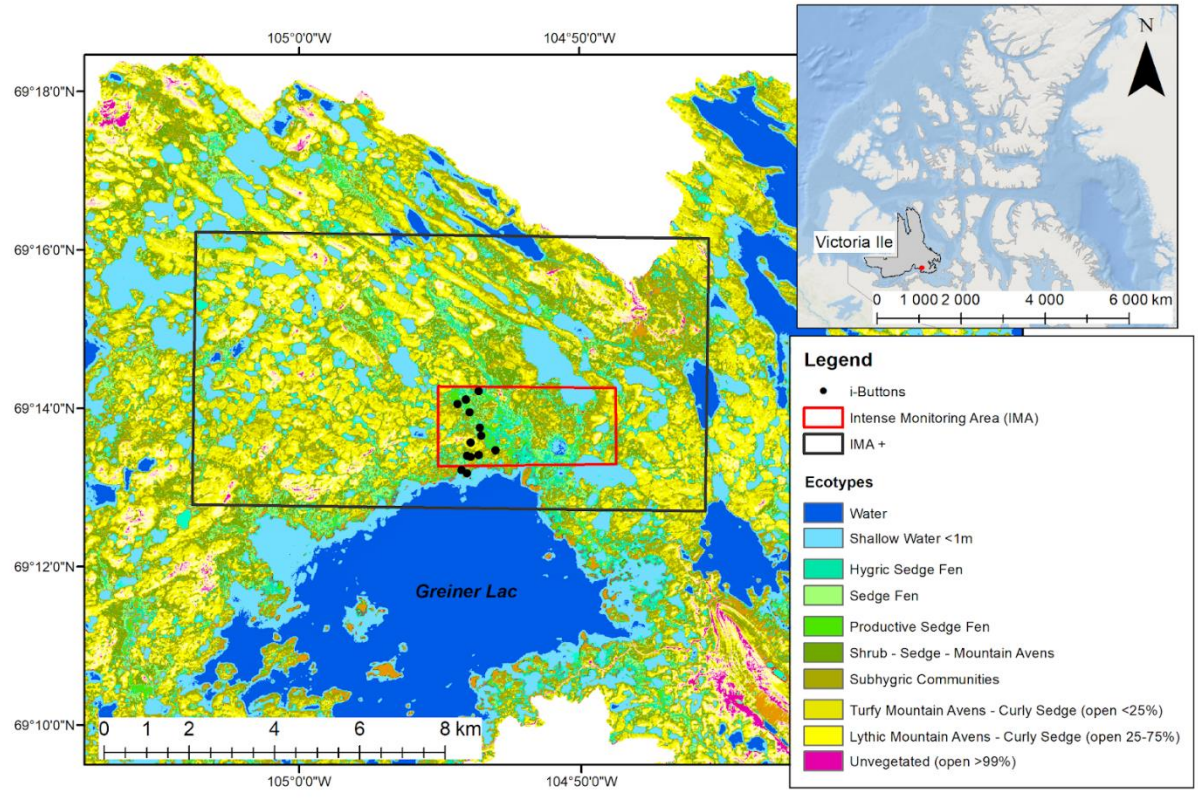

Figure 1: Study site of the IMA (red) and the extent covered by the F/T maps created in this study referred to as the IMA+ (black) near Cambridge Bay, Victoria Island, NU, with the ecotypes as a base map and i-Button locations. Legend of the ecotypes only includes dominant classes.

2.2 Data Description

2.2.1 Soil and air temperature

We developed and validated the F/T detection algorithm based on reference soil (T_{soil}) and air (T_{air}) temperature data (Figure 2.).

Soil Temperature: T_{soil} was measured using low-cost sensors (i-Buttons) deployed within the IMA over two years from July 2018 to mid-July 2019 in ten sites; and from mid-July 2019 to August 2020 in seven of the ten previous sites. The i-Buttons measured the soil temperature every three hours and have been placed at three depth ranges in the soil: from 2 cm to 4 cm; from 10 cm to 20 cm and from 20 cm to 30 cm in the following sites (IPX): *Hydric sedge fen* (IP2), *Sedge fen* (IP7, IP8 and IP14), *Productive sedge fen* (IP6 and IP11), *Subhygric communities* (IP5 and IP10), *Turfy mountain avens—Curly sedge (open <25%)* (IP15), and *Unvegetated (open >90%)* (IP13) as detailed in McLennan et al. (2018). Only the i-Buttons located at the

https://doi.org/10.5194/egusphere-2024-3580
Preprint. Discussion started: 23 January 2025

surface (first 4 cm of the soil) were used in the study, since C-band measurements are sensitive to changes near the surface and show limited soil penetration (Rowlandson et al., 2018). A fixed uncertainty of 0.5 ºC was considered on the data since the observed biases are within the manufacturer's precision (Prince et al., 2019). Soil temperatures were averaged daily since daily soil temperature variability is of the order of the i-Buttons uncertainty. The surface was considered frozen when T_{soil} ≤0.5 ºC and thawed when T_{soil} >0.5 ºC according to i-Button data, considering its accuracy and the clear zero curtain observed around 0 ºC during the freezing in fall (Figure 2). The zero curtain refers to the extended period during the freezing or thawing of the soil where the temperature stays around 0 ºC due to the release of the residual latent heat or water in the soil (Domine et al., 2018). Surface freezing (D_{fr}) and thawing (D_{th}) reference transition day of the year (DOY) were derived from the daily mean T_{soil}. $D_{fr(soil)}$ was defined as the first day of a series of 7 consecutive days when the surface was considered frozen for every i-Buttons, and $D_{th(soil)}$, as the first day of a series of 7 consecutive days considered thawed.

Air temperature: Average daily T_{air} data for 2018 to 2019 were obtained from the Environment and Climate Change Canada meteorological station (ECCC, https://climat.meteo.gc.ca/historical_data/search_historic_data_f.html) located at the Cambridge Bay airport, about 15 km from the IMA. Global reference transition DOY ($D_{th(air)}$ and $D_{fr(air)}$) were calculated from T_{air} as the first day of a series of 7 consecutive days classified as frozen (T_{air} ≤0 ºC) or thawed (T_{air} >0 ºC). Since T_{air} is considered constant over the study site, reference transition seasons were derived as +/- 30 days around $D_{th(air)}$ and $D_{fr(air)}$ (grey area in Figure 2).

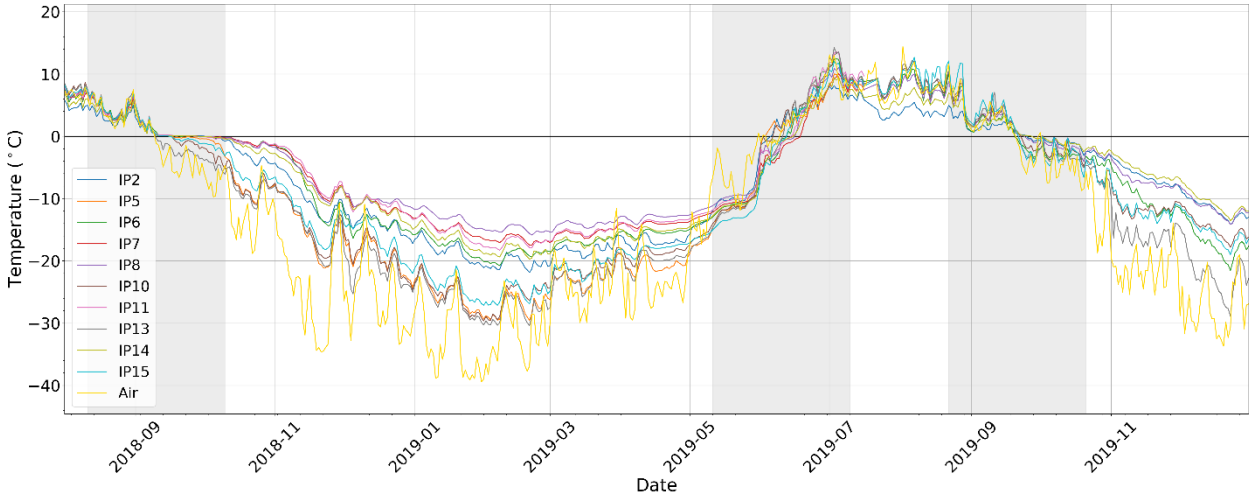

Figure 2: T_{soil} for the 10 reference sites (IP) and T_{air} from ECCC for the study period of August 2018 to December 2019 with the transition seasons (in grey) for freezing in 2018 and 2019 and thawing in 2019.

2.2.2 Synthetic Aperture Radar (SAR) dataset

In this study, we used the C-band (5.405 GHz) SAR backscatter obtained from the sensors of two satellite missions, namely the Sentinel-1A-1B constellation (available since 2016), and RADARSAT-2 (made available for this study between August

https://doi.org/10.5194/egusphere-2024-3580
Preprint. Discussion started: 23 January 2025

2018 to December 2019). Therefore, this study focuses on the period spanning from August 2018 to December 2019, where the overlap between both data source allows for quasi-daily revisit time in the transition seasons of Fall 2018 (F-2018), Spring 2019 (S-2019) and Fall 2019 (F-2019). Using both sensors, the average revisit times are respectively 1 day for F-2018 and F-2019, and approximately 2 days for S-2019 (see Table 2 in 3.1). Both datasets were preprocessed independently with a standardized processing chain (Section 3.1) and resampled to a standard 50 m × 50 m grid to be combined into one multisensor time series.

Sentinel-1A-1B: We used 270 Level-1 GRD Extra Wide Swath (EW) images from Sentinel-1A-1B in dual polarization (HH, HV) with a grid spacing of 40 m × 40 m. Due to the combination of measurements from multiple orbits, the acquisition incidence angles ranged from 20º to 46º. Descending/ascending scenes were used together.

RADARSAT-2: We used 200 *ScanSAR wide* SAR Georeferenced Fine product (SGF) RADARSAT-2 images in dual polarization (HH, HV) with a 50 m × 50 m grid spacing. We also used multiple orbits with an acquisition incidence angle ranging from 20º to 49º, including both descending and ascending scenes.

2.2.3 Ecotypes map

This study also presents a case study relying on a unique ecotype map created from unsupervised classification of 2011 WorldView-2 multispectral imagery (Ponomarenko et al., 2019) based on the Canadian arctic-subarctic Biogeoclimatic Ecosystem Classification (CASBEC) defined in McLennan et al., 2018. The CASBEC classification is based on terrestrial ecosystems (i.e., ecotypes) and includes vegetation characteristics, as well as the soil moisture regime (SMR). The ecotypes are mapped for Greiner Lake's watershed at a spatial resolution of 10 m and contain 19 map units regrouping 21 ecotypes. Resampling the 10 m × 10 m map to a 50 m × 50 m grid allowed to match the SAR imagery time series resolution. The analysis only included the pixels where 90% of the original 10 m x 10 m pixels within a 50 m x 50 m pixel have the same ecotype value. Waterbodies and ecotype classes with pixel count smaller than 20 were also excluded from the case study analysis. Table 1 present the number of pixels left from the resampling for the remaining ecotype classes. More details on the ecotypes can be found in Ponomarenko et al. (2019) from which a summary of the key characteristics relevant to this study are presented in Table 1: the soil moisture regime (SMR) and the maximal vegetation height. The soil moisture regime is defined by a scale ranging from 0 to 9, where 0 is very xeric and 9 is aquatic.

https://doi.org/10.5194/egusphere-2024-3580
Preprint. Discussion started: 23 January 2025

Table 1: Ecotypes classes found in the IMA+ and used inside the spatial analysis of F/T onset with soil moisture regime (SMR) and average vegetation height (Ponomarenko et al., 2019).

Classes	Soil moisture regime	Average vegetation height	Number of valid pixels
Lithic mountain avens—Curly sedge (open 75–90%)	2.5	5 cm	23
Lithic mountain—Curly sedge (open 25–75%)	3	5 cm	43
Turfy mountain avens—Curly sedge (open <25%)	4	5 cm	79
Subhygric communities	5	8 cm	80
Shrub—Sedge—Mountain avens	5.75	30 cm	37
Productive sedge fen	6.75	30 cm	326
Hydric sedge fen	8	30 cm	135

3 Methods

3.1 SAR processing

Both SAR datasets were preprocessed independently using a common chain (Figure 3), which includes radiometric calibration, speckle filtering, orthorectification and incidence angle normalization. First, we applied a radiometric calibration to the backscatter coefficient (σ^0). The calibration removed the dependency of the observation to the sensor characteristics; allowing us to combine the datasets from both sensors. To decrease spatial noise in each image, we then applied a Lee speckle filter with a window of 7 × 7 pixels. Finally, to allow the combination of dataset, images were then orthorectified to a fixed grid of 50 m × 50 m using a cubic interpolation method.

https://doi.org/10.5194/egusphere-2024-3580
Preprint. Discussion started: 23 January 2025

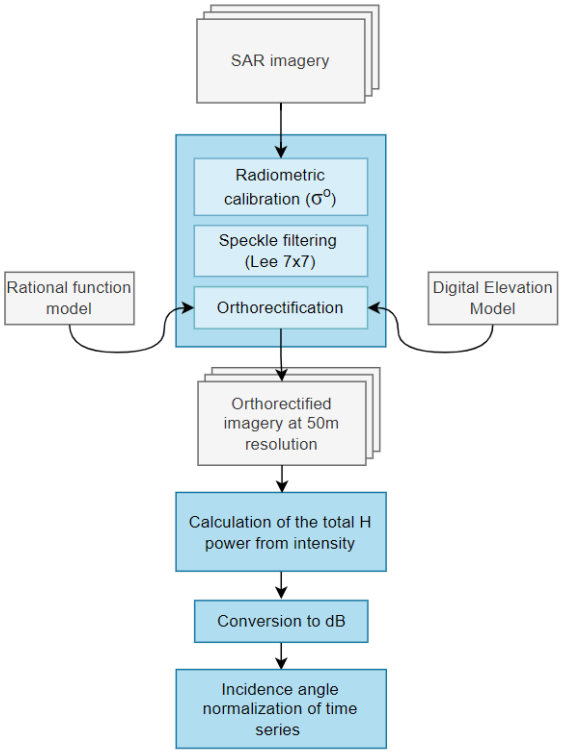

Figure 3: Flowchart of the SAR imagery (i.e., Sentinel-1 and RADARSAT-2) preprocessing.

Since this study focuses on dual polarization (i.e., horizontally transmitted, horizontally or vertically received), the total measured power in horizontal polarization (referred to as Total H power or HH+HV) then corresponds to the sum of both intensities (Woodhouse, 2006). The Total H power was calculated as one new time series and was used in the ecotype analysis (Section 3.4). The three time series (i.e., HH, HV and HH+HV) were then converted to decibels (dB).

Radar backscatter values were normalized for the different incidence angles of the various orbits used in this study. A linear regression between the backscatter coefficient (σ^0; in dB) and the incidence angle ($\theta_{incidence}$; in degrees) was calculated for each pixel independently such as

$$\sigma^{\circ}(\theta_{incidence}) = \alpha * \theta_{incidence} + \beta \quad (1)$$

where α represents the slope of the relation and β, the intercept (Chen et al., 2019; Makynen et al., 2002; Widhalm et al., 2018). During the thawed season, important changes in biomass and soil moisture levels influence the signal evolution. Therefore, the relationship between the incidence angle and the backscatter is less significant than in winter, where those changes are less likely to impact the backscatter between acquisitions (Chen et al., 2019). The α calculated from the regression using the backscatter during frozen period was then used to explain the year-round angular dependency for the datasets. The slope (α) was then calculated for each pixel independently for periods when the surface is considered completely frozen (DOY 1–60 for Sentinel-1, and DOY 305–365 and 1–60 for RADARSAT-2) for the combination of 2018, 2019 and 2020 when available. The

https://doi.org/10.5194/egusphere-2024-3580
Preprint. Discussion started: 23 January 2025

temporal periods for both sensors were chosen to get similar sample sizes for the same period. The time series were normalized at the median incidence angle of 34 ° as:

$$\sigma^{\circ}{}_{34} = \sigma^{\circ} - \alpha * (\theta_{incidence} - 34^{o}) \quad (2)$$

Sentinel-1 and RADARSAT-2 time series were then combined to create a multisensor time series with a quasi-daily mean temporal resolution for all three transition seasons (Table 2).

Table 2: Mean temporal resolution (in days) of the combined Sentinel-1/RADARSAT-2 normalized datasets for three transition seasons and for the whole time series (2018–2019).

	F-2018	S-2019	F-2019	2018–2019
Sentinel-1	2.2	3.2	1.9	2.2
RADARSAT-2	1.9	3.5	1.8	2.5
Multisensor	1.0	1.8	1.0	1.3

3.2 F/T detection algorithm

This study applies an empirical detection algorithm to identify the surface F/T state, using the same approach as the *SMAP L3 EASE-Grid Freeze/Thaw State* product (Derksen et al., 2017). The algorithm uses seasonal reference values to calculate a scale factor that is then classified into frozen or thawed state using a defined threshold (Rautiainen et al., 2016, 2014). Based on the work of Roy et al. (2015), using passive microwave data, we compared three methods to calculate seasonal reference values (Section 4.2.1). The first method ("average") uses the average backscatter coefficients for a period during which, based on soil and air temperature measurements, the soil is completely frozen (December 1, 2018, to April 1, 2019; σ_{fr}) or completely thawed (July 1, 2019, to September 1, 2019; σ_{th}). The second method ("median") uses the median backscatter coefficients over the same periods. Finally, the third method ("average-5") uses the average of the five lowest backscatter observations during the frozen period, and the average of the five highest backscatter values during the thawed period. Frozen (σ_{fr}) and thawed (σ_{th}) seasonal reference values are calculated for every pixel independently, and subsequently used to calculate the seasonal scale factor (Δ) for every observation at time *t* as:

$$\Delta(t) = \frac{\sigma(t) - \sigma_{fr}}{\sigma_{th} - \sigma_{fr}} \quad (3)$$

where $\sigma(t)$ is the backscattering coefficient for one pixel at time *t*. Each standardized $\Delta(t)$ values are then classified as frozen or thawed with a defined threshold (T) such that:

$$\begin{cases} \Delta(t) \leq T \rightarrow Frozen \\ \Delta(t) > T \rightarrow Thawed \end{cases} \quad (4)$$

The threshold (T) was optimized by calculating the accuracy of the classification for threshold values ranging between 0 and 1, at an increment of 0.01 using Eq. 5 on the ten reference sites. $D_{th\text{-}fr(sol)}$ and $D_{th\text{-}fr(air)}$ were used as reference values to calculate the amount of good observation (#good observation) for the classification with every increment of thresholds (Section 4.2.2).

https://doi.org/10.5194/egusphere-2024-3580
Preprint. Discussion started: 23 January 2025

$$Accuracy\ (\%) = \frac{\#good\ observation}{\#total\ of\ observations}\ \text{x}\ 100 \quad (5)$$

3.3 Case study

3.3.1 Surface F/T maps

The optimized threshold, defined with the ten reference sites, was then used to create the surface F/T maps covering the IMA and its surroundings (IMA+; Figure 1.). The algorithm was applied on a cell-by-cell basis to retrieve the transition onset for F-2018, F-2019 and S-2019. We applied a hydrographic mask to remove any non-terrestrial pixel. Pixels with equal or higher frozen than thawed reference values ($\sigma_{fr} \geq \sigma_{th}$) were also discarded. The temporal evolution of the backscatter in those cases did not allow for the detection of the dielectric discontinuity between soil state during the transition seasons, potentially linked to the presence of rocks of higher rugosity inside the pixels. Also, since T_{air} was considered constant across our study area, detected freezing and thawing dates falling outside the 60-day periods defined around $D_{th(air)}$ and $D_{fr(air)}$ were considered false detections, and were therefore discarded during the creation of the surface F/T maps. We chose to use the Total H power for the creation of the F/T maps to decrease the impact of the target orientation (e.g., vegetation distribution). Furthermore, by using this approach, we also increased the signal-to-noise ratio (SNR; Entekhabi et al., 2014), linked to the increase in signal quantity.

3.3.2 Ecotypes analysis

To analyze the impact of ecotypes on the surface F/T DOY, we compared the surface F/T maps derived from HH+HV to the resampled ecotypes map, and calculated the mean surface and standard deviation of surface F/T DOY per ecotype. A generalized least square model (GLS) was used to estimate values of surface freezing and thawing DOY per ecotype class with standard error. We created 3 models, one per transition season (freezing transition 2018 and 2019 and thawing transition 2019) for the Total H power dataset. A variance and spatial autocorrelation structure were defined in the models.. F/T transition DOY derived from the models were used to establish if the differences of the timing in transition DOY between ecotype class were statistically significant.

4 Results

4.1 Incidence angle normalization

Figure 4 compares the temporal evolution of backscatter with the same Sentinel-1 (Figure 4a, b) and RADARSAT-2 (Figure 4c, d) pixel, after the basic preprocessing (e.g., before incidence angle normalization) and after the incidence angle normalization. The incidence angle normalization decreases the noise in the temporal signature by reducing the impact of multiple orbits for a given pixel. It reduces the incidence angle dependency of each observation, allowing a greater distinction between freeze and thaw signals. For winter months, we found that the normalization, on average, decreased the signal standard

https://doi.org/10.5194/egusphere-2024-3580
Preprint. Discussion started: 23 January 2025

deviation by 39%, 46% and 33% for HH, HV and HH+HV polarizations for Sentinel-1 respectively, and by 37%, 84% and 37% for RADARSAT-2 at the ten reference sites. For summer months, that decrease was 48%, 88% and 46% for Sentinel-1, and 37%, 69% and 36% for RADARSAT-2.

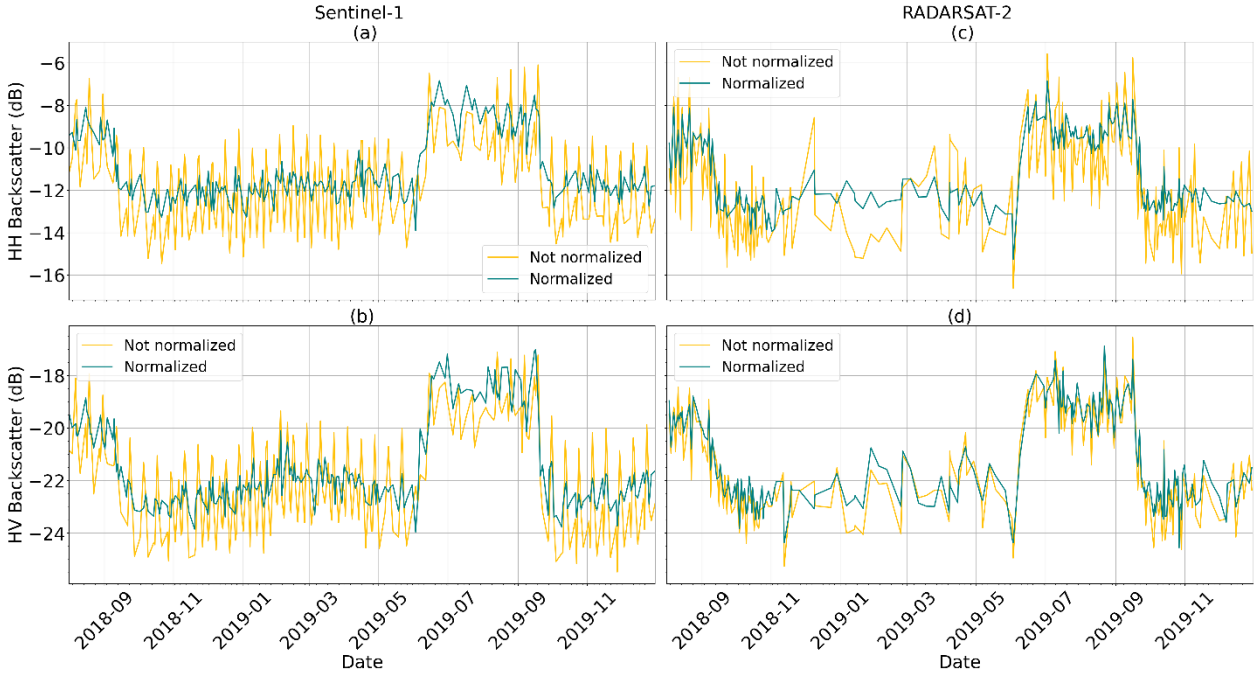

Figure 4: Examples of the backscatter time series for one pixel of Sentinel-1 and RADARSAT-2 data for the study period after basic preprocessing (yellow) and incidence angle normalization (green).

4.2 F/T detection algorithm development

As mentioned earlier, we evaluated three different methods to deduce the seasonal reference value for the algorithm (Section 4.2.1). A threshold optimization was conducted from the calculation of accuracy for increments of threshold between 0 and 1 (Section 4.2.2).

4.2.1 Comparison of the σ_{fr} and σt_h reference value

The two reference values σ_{fr} and σ_{th} were calculated independently for each of the reference sites. Table 3 shows that for the combination of the reference sites, the performance of the algorithm is not impacted by the approach used to determine the reference values over the complete study period, with a difference of less than 0.5% in detection accuracy. The same similarities were observed when calculating the accuracy per transition season for each reference value method. Those similarities between methods confirm that C-band signal can easily discern the two thermodynamic stages of the soil independently from the method chosen. Even though we observed close to no difference, the "average-5" method could be

https://doi.org/10.5194/egusphere-2024-3580
Preprint. Discussion started: 23 January 2025

more sensitive to the presence of residual noise or outlier backscatter measurements left in the time series, just as the "average" method could be. Therefore, we used the "median" method for the following analysis.

Table 3: Multisensor F/T detection highest accuracy (%) calculated with T_{soil} reference data, for the three reference values definitions of σ_{fr} and σ_t for the time series of 2018 to 2019.

		σ_{fr} and σ_{th} definition		
		Average	Median	Average-5
All 2018–2019	**HH**	96.9	96.9	96.9
	HV	97.5	97.5	97.4
	HH+HV	97.2	97.2	97.4

4.2.2 Threshold optimization

Figure 5 shows the accuracy of the detection algorithm as a function of the threshold between 0 and 1 (at a 0.01 increment) on HH, HV and HH+HV datasets. The accuracy is calculated for the ten reference sites combined, with T_{soil} (solid line) and T_{air} (dashed line) reference values over a) the entire time series; b) the freezing transition periods for 2018 and 2019 combined; and c) the thawing transitions for 2019. The algorithm applied over the entire time series (Figure 5a) suggests high accuracy (>95%) for threshold values ranging between 0.40 and 0.65 for all polarizations and temperature datasets. This overall classification accuracy provides a good initial assessment of the detection accuracy, but fails to assess the threshold behaviour during the surface F/T transition periods. Since the accuracy for classification values during summer and winter are close to 100% for a threshold close to 1 (i.e., summer) or 0 (i.e., winter). The number of "good" observations is thus increased, which decreases the weight of each individual value in the accuracy calculation (Eq. 5). Therefore, the data from August 11 to October 10, 2018, and August 21 to October 20, 2019, (i.e., freezing seasons) and May 11 to July 10, 2019 (i.e., thawing season) was extracted from the time series to evaluate the behaviour of the algorithm during those key periods of freezing and thawing. Figure 5b and c show the difference in the retrieval accuracy along the increment of thresholds during the freezing and thawing periods respectively. Results show that a clear threshold value maximizing the accuracy exists between 0.50 and 0.65 for the classification of the freezing period (Figure 5b) for all datasets. For the thawing transition, multiple threshold values across a larger range yield a high accuracy (Figure 5c). The signal classification during the thawing transition is largely insensitive to the threshold over a wide range of increments, where the accuracy remains mostly stable (0.2 to 0.6 for HH, 0.3 to 0.7 for HV and 0.2 to 0.7 for HH+HV polarization). A common threshold for both transition periods could then be considered for the surface F/T detection. Figure 5c also suggests that in the classification accuracy, the soil temperature performs better by almost 10% when compared to air temperature over the range of thresholds presented. We therefore chose the optimized threshold from the best accuracy compared to T_{soil} measurements for the combination of both transition seasons. A threshold of 0.56 was defined as maximizing the accuracy of transition seasons for HH polarization and of 0.53 for HV polarization (Table 4).

https://doi.org/10.5194/egusphere-2024-3580
Preprint. Discussion started: 23 January 2025

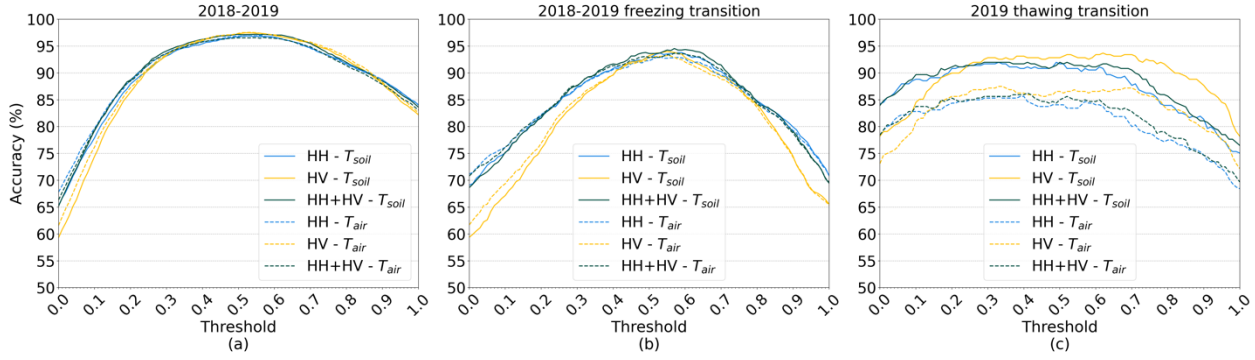

Figure 5: Accuracy of the seasonal algorithm over 0.01 increments on the threshold for (a) the entire time series of 2018 to 2019, (b) the freezing transition of 2018 and 2019, and (c) the thawing transition of 2019.

Since both polarizations show similar accuracy results for the F/T detection, the combination of the two polarizations also gives similar high results. The same threshold optimization was done on the Total H power time series and a threshold of 0.62 was found to optimize the accuracy of detection (Table 4).

Table 4: Accuracy for the combined transition period (F-2018, S-2019 and F-2019) with optimized threshold.

	Threshold	Accuracy of transition period
HH	0.56	93.1%
HV	0.53	93.8%
HH+HV	0.62	93.6%

4.3 Case study: impact of ecotype on surface F/T for a low arctic environment

We created surface F/T maps with the optimized threshold of 0.62 using the Total H power over the three transition seasons, yielding three maps (Fig. 6) for the IMA+, one for each transition season. Depending on the transition season, between 74% and 81% of the original area appear in those maps after applying the masks (see Section 3.3). Table 5 shows the mean DOY for freezing and thawing transition seasons from 2018 and 2019 with the standard deviation calculated from the maps. For average DOY detected, S-2019 shows a higher standard deviation than F-2018 and F-2019. Overall, we can see that in 2019, the soil froze around ten days later than in 2018.

https://doi.org/10.5194/egusphere-2024-3580
Preprint. Discussion started: 23 January 2025

Table 5: Mean transition day of year (DOY) for the IMA+ with standard deviation in brackets for the three transition seasons.

		Transition DOY
Freezing transition	2018	253.7 (2.6)
	2019	265.0 (2.1)
Thawing transition	2019	167.3 (3.9)

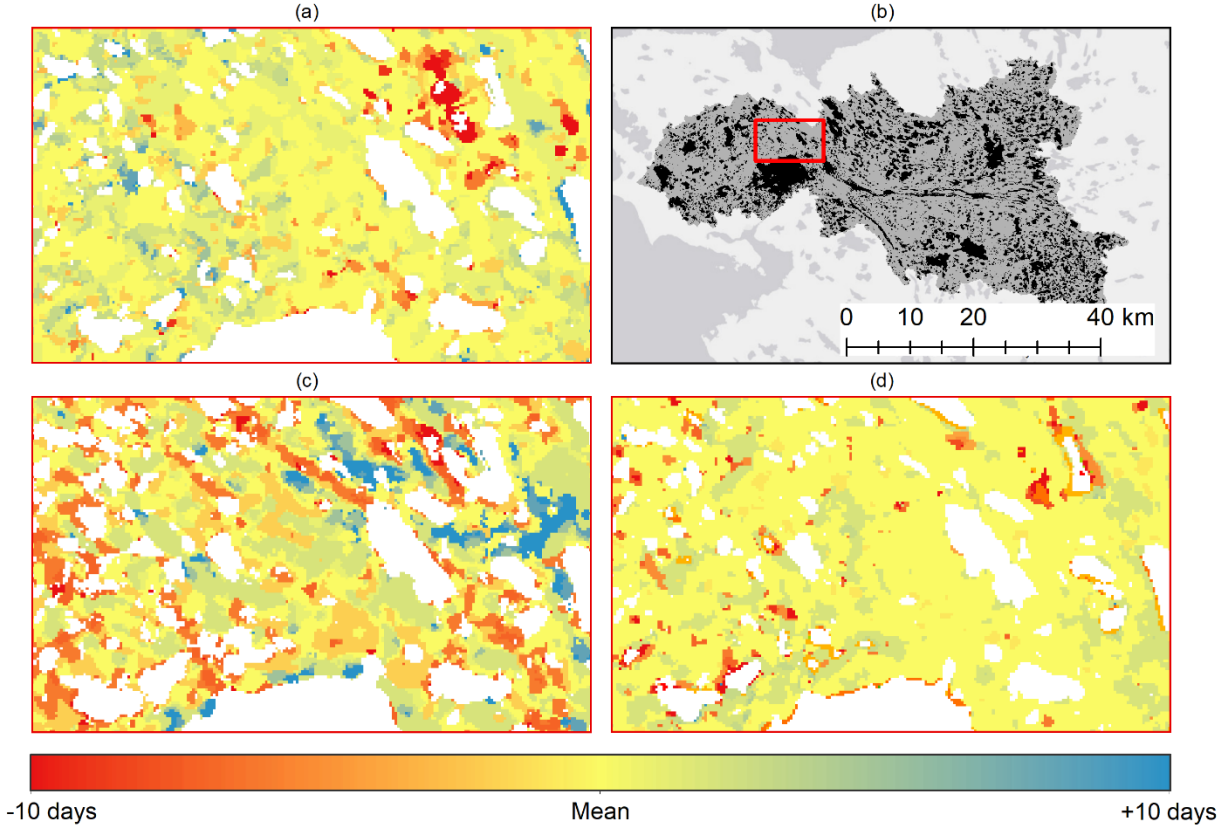

Figure 6: Freeze and thaw DOY maps for the IMA + area using HH+HV for F-2018 (a), S-2019 (c) and F-2019 (d). Areas without data appear in white. The ecotype data extent for the Greiner Lake watershed is shown in (b) with the F/T map extent in red.

We investigated potential relationships between surface F/T DOYs and ecotypes, given that different ecotypes have different soil and vegetation moisture levels (i.e., thermal conductivity) implying consequences on the surface F/T cycles. Table 6 shows the mean and standard deviation of freezing and thawing DOY defined with HH+HV over the three transition seasons per ecotype class. The range, which is quite small for all seasons, represents the difference between the mean surface F/T DOY of the first and the last ecotype to transition for each season.

https://doi.org/10.5194/egusphere-2024-3580
Preprint. Discussion started: 23 January 2025

Table 6: Mean and standard deviation of surface F/T DOY for each ecotype class using Total H power (HH+HV) for the three transition seasons. Ecotypes appear according to their soil moisture regime (SMR) from subxeric to hydric (i.e., dry to wet).

SMR	**Ecotype**	**F-2018**	**T-2019**	**F-2019**
Subxerix	Lithic mountain avens—Curly sedge (open 75–90%)	252.9 (3.1)	168.5 (3.3)	266.4 (4.1)
Submesic	Lithic mountain—Curly sedge (open 25–75%)	253.2 (1.9)	168.1 (3.7)	265.2 (2.2)
	Turfy mountain avens—Curly sedge (open <25%)	253.8 (1.2)	166.6 (4.7)	265.4 (2.5)
Subhygric	Subhygric communities	254.2 (2.6)	166.2 (4.4)	264.9 (0.8)
Hygric	Shrub—Sedge—Mountain avens	253.5 (1.8)	165.3 (2.0)	264.9 (0.5)
	Productive sedge fen	254.3 (1.0)	167.4 (2.8)	264.8 (0.7)
Hydric	Hydric sedge fen	255.2 (2.1)	166.7 (3.8)	264.9 (0.4)
	Range	2.4	3.2	1.7

Three GLS models were created to establish if a statistical difference exists between the surface F/T DOY of each ecotype classes per transition seasons. Fig. 7 shows the model estimates values for freezing (Fig. 7a, c) and thawing (Fig. 7b) transition seasons along with standard deviation. For F-2018, drier ecotypes tend to freeze sooner than hydric ecotypes, and for F-2019, only the class *Lithic Mountain avens—Curly sedge (Open 75–90%)* shows no overlap with the other classes. For the thawing transition season for 2019 (Fig. 9b), no clear trend is visible between the ecotypes but there is a clear difference between *Lithic mountain—Curly sedge (Open 25–75%)* and *Lithic Mountain avens—Curly sedge (Open 75–90%)* when compared with the other classes. Those drier and lower vegetation ecotypes (average 5 cm typical vegetation height) thaw later than the other more hydric and higher vegetation ecotypes (average 30 cm typical vegetation height).

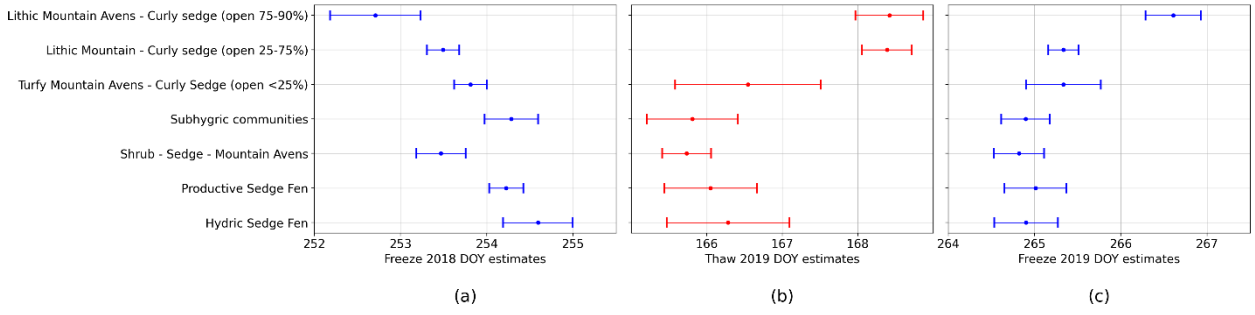

Figure 7: Estimated transition DOY from GLS models for 2018 freezing (a), 2019 thawing (b), and 2019 freezing (c) seasons with standard deviation per ecotypes classes.

https://doi.org/10.5194/egusphere-2024-3580
Preprint. Discussion started: 23 January 2025

5 Discussion

This study combined C-band SAR observations from Sentinel-1 and RADARSAT-2 sensors to create a quasi-daily time series, which delivers a spatially detailed surface F/T detection capacity and precision across an arctic tundra environment. The seasonal threshold algorithm was effective in classifying SAR backscatter observation into frozen or thawed states. The influence of the snow cover on the freezing transition and the differences between the freezing and thawing detection ability are now discussed, along with the impact of the low arctic environment ecotypes on the transition onset for the case study region.

5.1 Evaluation of the seasonal F/T algorithm

5.1.1 Impact of snow on freezing transition

The temporal evolution of T_{soil} for the reference sites is quite different for F-2018 and F-2019 due to different meteorological conditions during those freezing transitions. Fig. 8a and b show the temporal evolution of T_{soil} at two locations (IP8 and IP13) along with T_{air}. We chose the site IP8 and IP13 to illustrate the difference between moist and dry ecotypes respectively. The site IP8 is composed of a *Sedge fen* ecotype, which is a hydric ecosystem characterized as very moist to wet (McLennan et al., 2018). The clear zero-curtain effect in higher moisture ecotype is highlighted during F-2018 in IP8 (*Sedge fen*), with the soil temperature remaining close to 0 ºC over a longer period, before freezing completely (Domine et al., 2018). This is different compared to the drier IP13 site located in the *Unvegetated (open >99%)* ecotype. In addition to the difference due to soil moisture, we examined snow cover information from the *IMS Daily Northern Hemisphere Snow and Ice Analysis* (U.S. National Ice Center, 2008). This dataset provides information at 1 km to determine the snow onset (>40% coverage of 1 km) for these two transition seasons. We found that snow arrived almost one month later in 2019 (October 9, 2019) than in 2018 (September 11, 2018). The zero-curtain period is increased when snow covers the ground and isolates the soil from the cold air temperatures (Yi et al., 2018). We observed this with the soil temperature of the *Sedge fen* ecotype during F-2018 (Fig. 8a) when compared to the same location during F-2019 (Fig. 8b). On the other hand, the absence of snow cover increases cooling of the soil from the air, leading to a more direct freeze for both ecotypes (Fig. 8b). This is illustrated in Fig. 8b, when both i-Buttons freeze concurrently with T_{air} falling below freezing in F-2019. A clearer distinction between states is reflected in the C-band signal with a faster and greater decrease of backscatter between thawed and frozen soil in the F-2019 time series for both the *Sedge fen* and the unvegetated ecotype as shown in Fig. 8d compared to Fig. 8c. Interestingly, despite the difference in the soil moisture regime between the two sites, the backscattering trends are similar, with slightly higher σ^0 at IP13 in winter, probably related to the lower fraction of ice in the soil.

Furthermore, Fig. 8a shows that the decrease in the backscatter signal agrees with the start of the zero-curtain effect as measured at 2 cm in the soil. This result highlights that even though T_{soil} is not below zero, like for F-2018, the microwave signal decreases following the dielectric discontinuity of the soil surface when T_{soil} is close to 0 ºC, as observed in Rowlandson

https://doi.org/10.5194/egusphere-2024-3580
Preprint. Discussion started: 23 January 2025

et al., 2018, thus making the C-Band signal sensitive to the beginning of the zero curtain. Since the signal at C-band frequency is sensitive to the soil surface, we hypothesis that, at the beginning of the zero curtain and around 0 ºC, a thin frozen layer (i.e., a change in the water phase) appears at the very top of the soil, creating a dielectric discontinuity and thus resulting in a backscatter decrease. Also, we chose the i-Buttons location to be representative of a homogeneous patch of land cover. However, the SAR pixels cover a soil surface of 2 500 m^2. During F-2018, the start of the gradual backscatter decrease observed before T_{soil} reached 0 ºC could be explained by the averaging of the soil contribution inside the pixels. Indeed, the punctual measurements of T_{soil} do not represent the full extent covered by the pixels especially when isolating snow is present on the ground, increasing the zero-curtain effect for higher ground moisture (Domine et al., 2018).

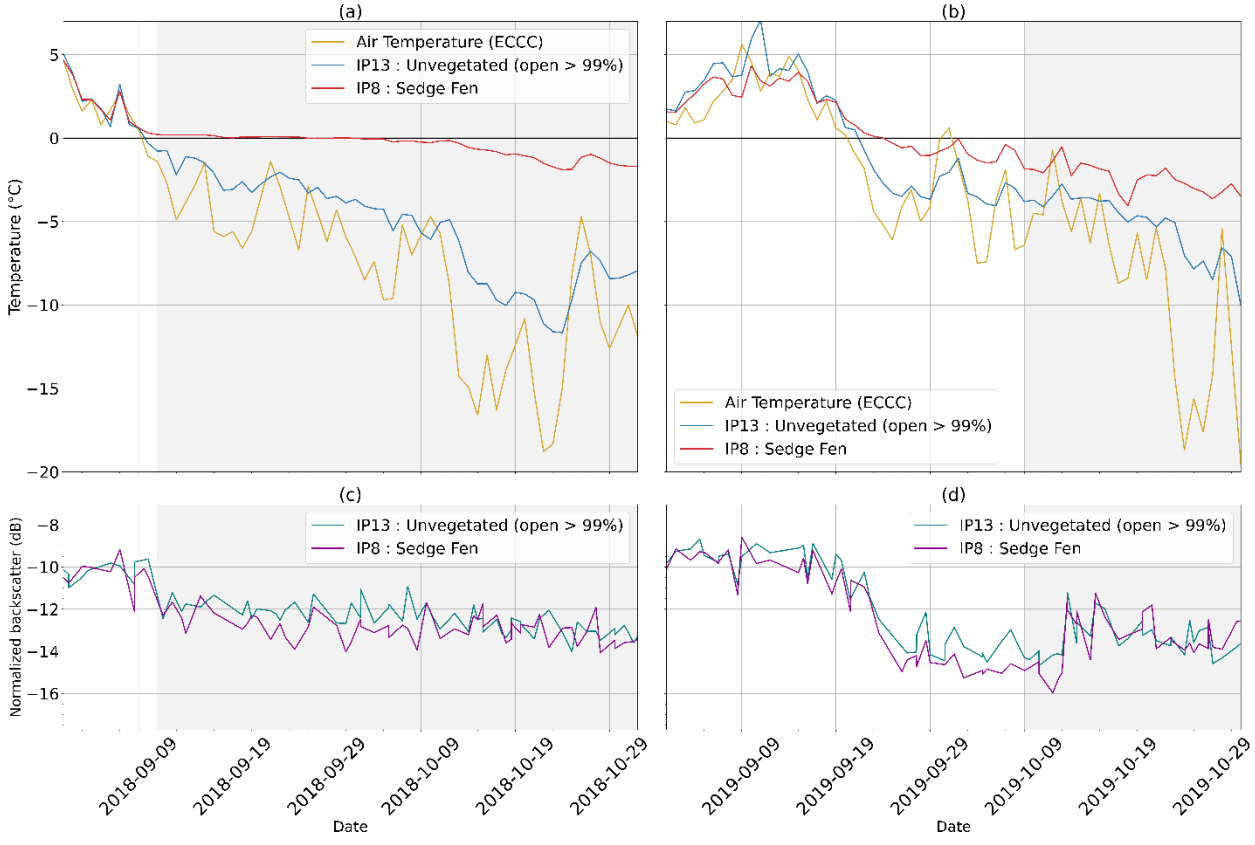

Figure 8: Surface soil temperature for two i-Buttons sites (IP8 and IP13) and air temperature (top) with HH+HV backscatter multisensor time series (bottom) for *Sedge fen* (IP8) site. Presence of snow on the ground is shown in grey for 2018 (left) and 2019 (right) freezing periods.

As for the detection capacity of the algorithm, the faster decrease in the signal, showing a clearer distinction between surface states, resulted in higher accuracies for F-2019 classification (Fig. 9), meaning less uncertainty in the detection, than for F-2018 for every threshold increment. Nonetheless, the C-band signal was sensitive to the freezing onset of the surface with a

https://doi.org/10.5194/egusphere-2024-3580
Preprint. Discussion started: 23 January 2025

decrease of 3–4 dB for the two fall seasons, with an accuracy higher than 93% independently from the presence of snow compared to T_{soil} reference values.

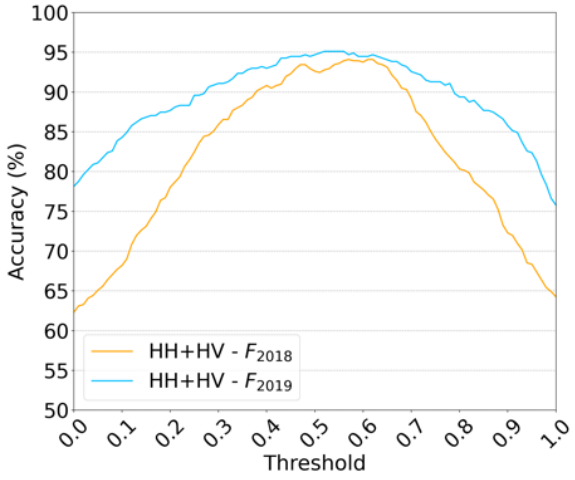

Figure 9: Accuracy, for every increment of threshold for HH+HV time series, for F-2018 and F-2019 independently.

5.1.2 Difference between freeze and thaw detection accuracy

Dividing the signal into freezing and thawing transition seasons during the threshold optimization showed a clear difference between the signal behavior for those two seasons, linked to the different processes driving those transitions. Regardless, Fig. 5b and 5c showed that we could use a common threshold definition for both transition seasons since, for the thawing classification, the accuracy is nearly independent from the change in threshold. This can be explained by the behavior of the signal during the thawing season, for which we observe a clear difference in backscatter between frozen and thawed surface. Generally, it is expected that the surface thaw onset happening under wet snow would be difficult to monitor, because wet snow is mostly opaque to microwave (i.e., surface scattering) (Ulaby et al., 1986). The dielectric properties of snow are defined in two distinct phases: (1) dry snow, having a low dielectric constant related to the absence of liquid water within it; and (2) wet snow, having a high dielectric constant related to the presence of liquid water in the air-ice mixture (Langlois et al., 2007). The C-band signal would then decrease with the presence of wet snow on the ground (Tsai et al., 2019), which decreases the penetration depth and increases the surface scattering of the air and snow interface as air temperatures rise above zero in the spring. In fact, in the SAR temporal series, the backscattering coefficient decreases when air temperature rises above 0 °C. However, that decrease is rather small because the backscatter of frozen tundra soil is already low. This signal intensity decrease is followed by a sharp increase of the order of 3–5 dB related to ground surface thawing. Hence, the increase in T_{air} during spring matches the start of snowmelt. However, our results show a strong agreement of this increase with soil temperature rising above 0 °C, suggesting, that the sharp backscatter increase is an indication of wet snow turning into exposed thawed soil. Even though the C-band signal is affected by the presence of wet snow on the ground, the fact that the wet snow

https://doi.org/10.5194/egusphere-2024-3580
Preprint. Discussion started: 23 January 2025

signal and the thawed soil seem to happen almost at the same time, could indicate that the detection of soil surface thawing during the spring using C-band SAR observations is possible considering the strong agreements obtained with the soil surface temperature in the Arctic's tundra environment. Nevertheless, to fully understand the thawing signal in such environment, the used of a more comprehensive dataset that include snow depth, snow temperature and snow liquid water content for different conditions (years and area) would be necessary. Studies using ground-based radar could also help to better understand the processes leading to the thawing signal in spring for arctic environments (King et al., 2018, Rowlandson et al., 2018).

5.2 Case study : Ecotypes effects on F/T DOY

The Total H power allows removal of the polarization dependency of the signal to the target. The modelled differences between ecotypes classes for the three transition seasons would therefore be due to the impact of different ecotypes on the surface thermal regime.

Freeze DOY: As discussed in Section 5.1.1, the presence of snow on the ground increased the zero curtain during fall. It creates a bigger gap between freezing DOY from different moisture level soil during F-2018, and in contrast, the absence of snow on the ground during F-2019 leads to a more homogeneous freeze across all ecotypes (Table 6) as detected. The estimated value from the GLS models for the F-2019 dataset shows that the difference between classes is not significant for almost all classes, except for the class *Lithic mountain avens—Curly sedge (Open 75–90%)*. Once again, considering the sensitivity of the signal to the water phase change at the soil surface, those similarities could be linked to the absence of snow on the ground, making the soil surface more sensitive to the cooling of air temperature, regardless of the soil moisture level or ecotype. For F-2018, as shown earlier in Fig. 9a, the difference between ecotype in freezing DOY is strongly linked to the moisture level of the soil. As discussed earlier, a higher moisture soil tends to freeze later than a drier soil due to the presence of more latent heat linked to the presence of water, and this difference is increased by the presence of an insulating snowcover.

Thaw DOY: For the thawing transition, the model estimated that drier ecotypes with lower vegetation thaw later than ecotypes with higher moisture and vegetation. Higher vegetation increases trapping of the snow, resulting in deeper snow cover (Sturm et al., 2001, 2005) which insulates the ground more effectively from the cooling of the air. Furthermore, the presence of higher vegetation increases the creation of depth hoar, which is an even more insulative snow cover (Domine et al., 2016). Sturm et al. (2005) suggested that deeper snow cover result in higher soil temperature throughout winter. Moreover, Domine et al. (2021) found that the branches buried in the snow cover absorb solar radiation under the snow and conduct heat to the ground, resulting in earlier thaw for vegetated areas. That could explain the faster thaw observed for higher vegetation ecotypes. We could then hypothesize that the difference observed in the thawing DOY is linked to vegetation.

https://doi.org/10.5194/egusphere-2024-3580
Preprint. Discussion started: 23 January 2025

6 Conclusion

In this study, we applied C-band SAR data from multiple sensors to develop an algorithm to estimate freezing and thawing onset of the soil surface in an arctic environment near Cambridge Bay, NU. To analyze the potential of C-band SAR quasi-daily time series for soil surface F/T onset detection in the low arctic tundra, we used the seasonal threshold algorithm defined in Derksen et al. (2017) and Rautiainen et al. (2016) with an optimized threshold. As a case study, we then evaluated the impact of ecotypes on the surface F/T DOY onset across the study site by comparing the surface F/T maps created from the Total H power (i.e., HH+HV) time series to ecotypes maps created by McLennan et al. (2018).

Normalizing the incidence angle of the signal for both sensors helped to minimize noise in time series that combinesmultiple orbits of observation, and therefore provides an improved distinction between soil states. Likewise preprocessing the Sentinel-1 and RADARSAT-2 imagery allowed to combine the two datasets to create a multisensor time series with a revisit time of just above one day for the key transition seasons of late 2018 and 2019. Since earlier studies have already suggested the spatial heterogeneity of the soil F/T, we had hypothesized that the spatial resolution (i.e., 50 × 50 m) of the SAR imagery would notably improve the retrieval of the spatial variability for the F/T onset transition when compared to passive microwave approaches. Parameterizing the seasonal threshold algorithm using T_{soil} reference data from multiple sites produced an overall detection accuracy of over 96% for the whole time series, and over 91% for every transition period. To create surface F/T onset maps of the IMA+, we used the threshold defined with the accuracy optimization on surface T_{soil} for the reference sites. Giving that soil type, moisture level and vegetation height directly impact the soil thermal regime, we hypothesized that the ecotype classes influence the soil surface F/T onset according to their characteristics. Results from the coupling of the surface F/T DOY maps with the ecotypes maps showed that differences between some ecotype classes are linked to moisture levels during freezing and to the presence of vegetation during thawing.

Overall, this study demonstrated the capacity of C-band SAR backscatter intensity to detect surface F/T in the tundra environment. Note that the signal of wet snow limits accurate thawing transition detection. For future use of the algorithm, backscatter reference values (σ_{fr} and σ_{th}) used inside the seasonal threshold algorithm could be updated by adding the new data for each year to decrease the impact of individual seasons. Also, average snow depth per ecotypes could help to validate if the retrieved thaw DOY is more linked to the presence of vegetation or snow cover. The surface F/T product created from this study demonstrates how, on one hand, the SAR backscatter can be used for surface F/T detection in low vegetation and shallow snow-covered terrain, and on the other hand, how it could be used as complementary data to improve modelling of the soil thermal regime.

https://doi.org/10.5194/egusphere-2024-3580
Preprint. Discussion started: 23 January 2025

Author contribution

Conceptualization, A.L., A.R. and C.D.; methodology, C.C., A.R. and A.L.; formal analysis, C.C..; data curation, C.C; writing—original draft preparation, C.C.; writing—review and editing, A.L, A.R. and C.D.; supervision, A.L. and A.R.; project administration, A.L.; funding acquisition, A.L. All authors have read and agreed to the published version of the manuscript.

Competing interest

At least one of the (co-)authors is a member of the editorial board of The Cryosphere

Acknowledgment

We would like to thank the Canada Centre for Mapping and Earth Observation (CCMEO) from Natural Resources Canada (NRCAN) for providing RADARSAT-2 imagery. This work was funded by the Natural Sciences and Engineering Research Council of Canada (NSERC), the Fonds de recherche du Québec—Nature et Technologies (FRQNT), Polar Knowledge Canada, Environment and Climate Change Canada (ECCC), the Northern Scientific Training Program (NSTP) and the Canadian Space Agency (CSA; FAST2019). We would like to thank the staff from the Canadian High Arctic Research Station (CHARS) and the community of Iqaluktuttiaq for their help and their tremendous logistical support during fieldwork, along with Alex Mavrovic, for the placement and retrieval of the i-Buttons in the IMA.

References

Miller, B. B. and Carter, C.: The test article, J. Sci. Res., 12, 135–147, doi:10.1234/56789, 2015.

Smith, A. A., Carter, C., and Miller, B. B.: More test articles, J. Adv. Res., 35, 13–28, doi:10.2345/67890, 2014.

Baghdadi, N., Bazzi, H., el Hajj, M. and Zribi, M.: Detection of Frozen Soil Using Sentinel-1 SAR Data. Remote Sensing 10. doi:10.3390/rs10081182, 2018.

Barrere, M., Domine, F., Belke-Brea, M. and Sarrazin, D.: Snowmelt Events in Autumn Can Reduce or Cancel the Soil Warming Effect of Snow–Vegetation Interactions in the Arctic, Journal of Climate, 31, 9507–9518. doi:10.1175/JCLI-D-18-0135.1, 2018.

Bjorkman, A.D., Myers-Smith, I.H., Elmendorf, S.C., Normand, S., Rüger, N., Beck, P.S.A., Blach-Overgaard, A., Blok, D., Cornelissen, J.H.C., Forbes, B.C., Georges, D., Goetz, S.J., Guay, K.C., Henry, G.H.R., HilleRisLambers, J., Hollister, R.D., Karger, D.N., Kattge, J., Manning, P., Prevéy, J.S., Rixen, C., Schaepman-Strub, G., Thomas, H.J.D., Vellend, M., Wilmking, M., Wipf, S., Carbognani, M., Hermanutz, L., Lévesque, E., Molau, U., Petraglia, A., Soudzilovskaia, N.A., Spasojevic, M.J., Tomaselli, M., Vowles, T., Alatalo, J.M., Alexander, H.D., Anadon-Rosell, A., Angers-Blondin, S., Beest, M. te, Berner, L., Björk, R.G., Buchwal, A., Buras, A., Christie, K., Cooper, E.J., Dullinger, S., Elberling, B., Eskelinen, A., Frei, E.R., Grau, O., Grogan, P., Hallinger, M., Harper, K.A., Heijmans, M.M.P.D., Hudson, J., Hülber, K., Iturrate-Garcia, M., Iversen, C.M., Jaroszynska, F., Johnstone, J.F., Jørgensen, R.H., Kaarlejärvi, E., Klady, R., Kuleza, S., Kulonen, A., Lamarque, L.J., Lantz,

https://doi.org/10.5194/egusphere-2024-3580
Preprint. Discussion started: 23 January 2025

T., Little, C.J., Speed, J.D.M., Michelsen, A., Milbau, A., Nabe-Nielsen, J., Nielsen, S.S., Ninot, J.M., Oberbauer, S.F., Olofsson, J., Onipchenko, V.G., Rumpf, S.B., Semenchuk, P., Shetti, R., Collier, L.S., Street, L.E., Suding, K.N., Tape, K.D., Trant, A., Treier, U.A., Tremblay, J.P., Tremblay, M., Venn, S., Weijers, S., Zamin, T., Boulanger-Lapointe, N., Gould, W.A., Hik, D.S., Hofgaard, A., Jónsdóttir, I.S., Jorgenson, J., Klein, J., Magnusson, B., Tweedie, C., Wookey, P.A., Bahn, M., Blonder, B., van Bodegom, P.M., Bond-Lamberty, B., Campetella, G., Cerabolini, B.E.L., Chapin, F.S., Cornwell, W.K., Craine, J., Dainese, M., de Vries, F.T., Díaz, S., Enquist, B.J., Green, W., Milla, R., Niinemets, Ü., Onoda, Y., Ordoñez, J.C., Ozinga, W.A., Penuelas, J., Poorter, H., Poschlod, P., Reich, P.B., Sandel, B., Schamp, B., Sheremetev, S. and Weiher, E.: Plant functional trait change across a warming tundra biome, Nature, 562, 57–62. doi:10.1038/s41586-018-0563-7, 2018.

Bourbigot, M., Johnsen, H., Piantanida, R., Hajduch, G., Poullaouec, J., 2016. Sentinel-1 Product Definition.

Brown, R., Vikhamar Schuler, D., Bulygina, O., Derksen, C., Luojus, K., Mudryk, L., Wang, L., and Yang, D.: Chapter 3. In: Snow, Water, Ice and Permafrost in the Arctic (SWIPA) 2017. pp. [26-55]. Arctic Monitoring and Assessment Programme (AMAP), Oslo, Norway, 2017.

Busseau, B.C., Royer, A., Roy, A., Langlois, A., and Domine, F.: Analysis of snow-vegetation interactions in the low Arctic-Subarctic transition zone (northeastern Canada). Physical Geography, 38, 159–175, doi:10.1080/02723646.2017.1283477, 2017.

Callaghan, T. v, Johansson, M., Brown, R.D., Groisman, P.Ya., Labba, N., Radionov, V., Bradley, R.S., Blangy, S., Bulygina, O.N., Christensen, T.R., Colman, J.E., Essery, R.L.H., Forbes, B.C., Forchhammer, M.C., Golubev, V.N., Honrath, R.E., Juday, G.P., Meshcherskaya, A. v, Phoenix, G.K., Pomeroy, J., Rautio, A., Robinson, D.A., Schmidt, N.M., Serreze, M.C., Shevchenko, V.P., Shiklomanov, A.I., Shmakin, A.B., Sköld, P., Sturm, M., Woo, M., and Wood, E.F.: Multiple Effects of Changes in Arctic Snow Cover, AMBIO, 40, 32–45, doi:10.1007/s13280-011-0213-x, 2011

Chen, R.H., Tabatabaeenejad, A., Moghaddam, M.: Retrieval of Permafrost Active Layer Properties Using Time-Series P-Band Radar Observations, IEEE Transactions on Geoscience and Remote Sensing, 57, 8, 6037-6054, doi:10.1109/TGRS.2019.2903935, 2019.

Chen, X., Liu, L., and Bartsch, A.: Detecting soil freeze/thaw onsets in Alaska using SMAP and ASCAT data, Remote Sensing of Environment, 220, 59–70, doi.10.1016/j.rse.2018.10.010, 2019

Cohen, J., Rautiainen, J.L., Smolander, T., Vehviläinen, J., and Pulliainen, J.: Sentinel-1 based soil freeze/thaw estimation in boreal forest environments, Remote Sensing of Environment, 254, 112267, doi.10.1016/j.rse.2020.112267, 2021.

Dai, A., Luo, D., Song, M. and Liu, J.: Arctic amplification is caused by sea-ice loss under increasing CO2, Nature Communications, 10, 121. doi.10.1038/s41467-018-07954-9, 2019.

Derksen, C., and Brown, R.: Spring snow cover extent reductions in the 2008-2012 period exceeding climate model projections, Geophysical Research Letters, 39, doi.10.1029/2012GL053387, 2012.

Derksen, C., Xu, X., Scott Dunbar, R., Colliander, A., Kim, Y., Kimball, J.S., Black, T.A., Euskirchen, E., Langlois, A., Loranty, M.M., Marsh, P., Rautiainen, K., Roy, A., Royer, A., and Stephens, J.: Retrieving landscape freeze/thaw state from

https://doi.org/10.5194/egusphere-2024-3580
Preprint. Discussion started: 23 January 2025

Soil Moisture Active Passive (SMAP) radar and radiometer measurements, Remote Sensing of Environment, 194, 48–62. doi.10.1016/j.rse.2017.03.007, 2017.

Domine, F., Barrere, M., and Morin, S.: The growth of shrubs on high Arctic tundra at Bylot Island: Impact on snow physical properties and permafrost thermal regime, Biogeosciences, 13, 6471–6486. doi.10.5194/bg-13-6471-2016, 2016.

Domine, F., Belke-Brea, M., Sarrazin, D., Arnaud, L., Barrere, M., and Poirier, M.: Soil moisture, wind speed and depth hoar formation in the Arctic snowpack, Journal of Glaciology, 64, 990–1002, doi./10.1017/jog.2018.89, 2018.

Domine, F., Picard, G., Morin, S., Barrere, M., Madore, J.B., and Langlois, A.: Major Issues in Simulating Some Arctic Snowpack Properties Using Current Detailed Snow Physics Models: Consequences for the Thermal Regime and Water Budget of Permafrost, Journal of Advances in Modeling Earth Systems, 11, 34–44, doi.10.1029/2018MS001445, 2018.

Domine, F., Fourteau, K., Picard, G., Lackner, G., Sarrazin, D., and Poirier, M.: Permafrost cooled in winter by thermal bridging through snow-covered shrub branches, Nature Geoscience, 15, 554-560, doi.10.21203/rs.3.rs-679013/v1, 2022.

Entekhabi, D. et al., 2014 SMAP Handbook–Soil Moisture Active Passive: Mapping Soil Moisture and Freeze/Thaw from Space.

Jeong, D., and Sushama, L.: Rain-on-snow events over North America based on two Canadian regional climate models. Climate Dynamics, 50, 303–316, doi.10.1007/s00382-017-3609-x, 2018.

Jagdhuber, T., Stockamp, J., Hajnsek, I., and Ludwig, R.: Identification of soil freezing and thawing states using SAR polarimetry at C-band, Remote Sensing 6, 2008–2023, doi.10.3390/rs6032008. 2014.

Kim, Y., Kimball, J.S., McDonald, K.C., and Glassy, J.: Developing a global data record of daily landscape freeze/thaw status using satellite passive microwave remote sensing, IEEE Transactions on Geoscience and Remote Sensing, 49, 949–960, doi.10.1109/TGRS.2010.2070515, 2011.

Kim, Y., Kimball, J.S., Zhang, K., and McDonald, K.C.: Satellite detection of increasing Northern Hemisphere non-frozen seasons from 1979 to 2008: Implications for regional vegetation growth, Remote Sensing of Environment, 121, 472–487. doi.10.1016/j.rse.2012.02.014, 2012.

King, J., Derksen, C., Toose, P., Langlois, L., Larsen, C., Lemmetyinen, J., Marsh, P., Montpetit, B., Roy, A., Rutter, N., and Sturm, M.: The influence of snow microstructure on dual-frequency radar measurements in a tundra environment, Remote Sensing of Environment, 215, 242-254, doi.10.1016/j.rse.2018.05.028, 2018.

Langlois, A., Barber, D.G., and Hwang, B.J.: Development of a winter snow water equivalent algorithm using in situ passive microwave radiometry over snow-covered first-year sea ice, Remote Sensing of Environment, 106, 75–88, doi.10.1016/j.rse.2006.07.018, 2007.

Langlois, A., Johnson, C.A., Montpetit, B., Royer, A., Blukacz-Richards, E.A., Neave, E., Dolant, C., Roy, A., Arhonditsis, G., Kim, D.K., Kaluskar, S., and Brucker, L.: Detection of rain-on-snow (ROS) events and ice layer formation using passive microwave radiometry: A context for Peary caribou habitat in the Canadian Arctic, Remote Sensing of Environment, 189, 84–95, doi.10.1016/j.rse.2016.11.006, 2017

https://doi.org/10.5194/egusphere-2024-3580
Preprint. Discussion started: 23 January 2025

Mäkynen, M.P., Manninen, A.T., Similä, M.H., Karvonen, J.A., Hallikainen, M.T.: Incidence Angle Dependence of the Statistical Properties of C-Band HH-Polarization Backscattering Signatures of the Baltic Sea Ice, IEEE Transactions on Geoscience and Remote Sensing, 40, 2593–2605, doi.10.1109/TGRS.2002.806991, 2002.

Martin, A.C., Jeffers, E.S., Petrokofsky, G., Myers-Smith, I., and MacIas-Fauria, M.: Shrub growth and expansion in the Arctic tundra: An assessment of controlling factors using an evidence-based approach, Environmental Research Letters, 12, doi.10.1088/1748-9326/aa7989, 2017.

McLennan, D.S., MacKenzie, W.H., Meidinger, D., Wagner, J., and Arko, C.: A Standardized Ecosystem Classification for the Coordination and Design of Long-term Terrestrial Ecosystem Monitoring in Arctic-Subarctic Biomes, Arctic, 71, 1–15, doi.10.14430/arctic4621, 2018

Park, S.-E., Bartsch, A., Sabel, D., Wagner, W., Naeimi, V., and Yamaguchi, Y.: Monitoring freeze/thaw cycles using ENVISAT ASAR Global Mode, Remote Sensing of Environment, 115, 3457–3467, doi.10.1016/j.rse.2011.08.009, 2011.

Ponomarenko, S., McLennan, D., Pouliot, D., and Wagner, J.: High Resolution Mapping of Tundra Ecosystems on Victoria Island, Nunavut–Application of a Standardized Terrestrial Ecosystem Classification, Canadian Journal of Remote Sensing 45, 551–571, doi.10.1080/07038992.2019.1682980, 2019.

Prince, M., Roy, A., Brucker, L., Royer, A., Kim, Y., and Zhao, T.: Northern hemisphere surface freeze-thaw product from aquarius L-band radiometers, Earth System Science Data, 10, 2055–2067, doi.10.5194/essd-10-2055-2018, 2018.

Prince, M., Roy, A., Royer, A., and Langlois, A.: Timing and spatial variability of fall soil freezing in boreal forest and its effect on SMAP L-band radiometer measurements, Remote Sensing of Environment, 231, doi.10.1016/j.rse.2019.111230, 2019.

Rautiainen, K., Lemmetyinen, J., Schwank, M., Kontu, A., Ménard, C.B., Mätzler, C., Drusch, M., Wiesmann, A., Ikonen, J., and Pulliainen, J.: Detection of soil freezing from L-band passive microwave observations, Remote Sensing of Environment, 147, 206–218, doi.10.1016/j.rse.2014.03.007, 2014.

Rautiainen, K., Parkkinen, T., Lemmetyinen, J., Schwank, M., Wiesmann, A., Ikonen, J., Derksen, C., Davydov, S., Davydova, A., Boike, J., Langer, M., Drusch, M., and Pulliainen, J.: SMOS prototype algorithm for detecting autumn soil freezing, Remote Sensing of Environment, 180, 346–360, doi.10.1016/j.rse.2016.01.012, 2016.

Rowlandson, T.L., Berg, A.A., Roy, A., Kim, E., Pardo Lara, R., Powers, J., Lewis, K., Houser, P., McDonald, K., Toose, P., Wu, A., de Marco, E., Derksen, C., Entin, J., Colliander, A., Xu, X., and Mavrovic, A.: Capturing agricultural soil freeze/thaw state through remote sensing and ground observations: A soil freeze/thaw validation campaign, Remote Sensing of Environment, 211, 59–70, doi.10.1016/j.rse.2018.04.003, 2018.

Roy, A., Royer, A., Derksen, C., Brucker, L., Langlois, A., Mialon, A., and Kerr, Y.H.: Evaluation of Spaceborne L-Band Radiometer Measurements for Terrestrial Freeze/Thaw Retrievals in Canada, IEEE Journal of Selected Topics in Applied Earth Observations and Remote Sensing, 8, 4442–4459, doi.10.1109/JSTARS.2015.2476358, 2015

https://doi.org/10.5194/egusphere-2024-3580
Preprint. Discussion started: 23 January 2025

Roy, A., Toose, P., Mavrovic, A., Pappas, C., Royer, A., Derksen, C., Berg, A., Rowlandson, T., El-Amine, M., Barr, A., Black, A., Langlois, A., and Sonnentag, O.: L-Band response to freeze/thaw in a boreal forest stand from ground- and tower-based radiometer observations, Remote Sensing of Environment, 237, doi.10.1016/j.rse.2019.111542, 2020.

Royer, A., Domine, F., Roy, A., Langlois, A., Marchand, N., and Davesne, G.: New northern snowpack classification linked to vegetation cover on a latitudinal mega-transect across northeastern Canada, Écoscience, 28, 225–242, doi.10.1080/11956860.2021.1898775, 2021.

Schuur, E.A.G., McGuire, A.D., Schädel, C., Grosse, G., Harden, J.W., Hayes, D.J., Hugelius, G., Koven, C.D., Kuhry, P., Lawrence, D.M., Natali, S.M., Olefeldt, D., Romanovsky, V.E., Schaefer, K., Turetsky, M.R., Treat, C.C., and Vonk, J.E.: Climate change and the permafrost carbon feedback, Nature, 520, 171–179, doi.10.1038/nature14338, 2015

Serreze, M.C., and Barry, R.G.: Processes and impacts of Arctic amplification: A research synthesis, Global and Planetary Change, 77, 85–96, doi.10.1016/j.gloplacha.2011.03.004, 2011.

Smith, S.L., Romanovsky, V.E., Lewkowicz, A.G., Burn, C.R., Allard, M., Clow, G.D., Yoshikawa, K., and Throop, J.: Thermal state of permafrost in North America: A contribution to the international polar year, Permafrost and Periglacial Processes, 21, 117–135, doi.10.1002/ppp.690, 2010.

Sturm, M., McFadden, J.P., Liston, G.E., Stuart Chapin, F., Racine, C.H., and Holmgren, J.: Snow-shrub interactions in Arctic Tundra: A hypothesis with climatic implications, Journal of Climate, 14, 336–344, doi.10.1175/1520-0442(2001)014<0336:SSIIAT>2.0.CO;2, 2011.

Sturm, M., Schimel, J., Michaelson, G., Welker, J.M., Oberbauer, S.F., Liston, G.E., Fahnestock, J., and Romanovsky, V.E.: Winter biological processes could help convert arctic tundra to shrubland, BioScience, 55, 17–26, doi.10.1641/0006-3568(2005)055[0017:WBPCHC]2.0.CO;2, 2005.

Tsai, Y.L.S., Dietz, A., Oppelt, N., and Kuenzer, C.: Remote sensing of snow cover using spaceborne SAR: A review, Remote Sensing, 11, doi.10.3390/rs11121456, 2019

Ulaby, F.T., Moore, R.K., and Fung, A.K.: Microwave Remote Sensing: Active and Passive, vol. III, Volume Scattering and Emission Theory, Advanced Systems and Applications. Inc., Dedham, Massachusetts, USA: Norwood, Massachusetts: Artech House, 1986.

U.S. National Ice Center. updated daily. IMS Daily Northern Hemisphere Snow and Ice Analysis at 1 km, 4 km, and 24 km Resolutions, Version 1. [1 km]. Boulder, Colorado USA. NSIDC: National Snow and Ice Data Center. doi: https://doi.org/10.7265/N52R3PMC. May 2021. 2008.

Wang, G., Hu, H., and Li, T.: The influence of freeze-thaw cycles of active soil layer on surface runoff in a permafrost watershed, Journal of Hydrology, 375, 438–449, doi.10.1016/j.jhydrol.2009.06.046, 2009.

Widhalm, B., Bartsch, A., and Goler, R.: Simplified normalization of C-band synthetic aperture radar data for terrestrial applications in high latitude environments, Remote Sensing, 10, 1–18, doi.10.3390/rs10040551, 2018.

Woodhouse, I.H.: Introduction to Microwave Remote Sensing (1st ed.). CRC Press, 400 p. https://doi.org/10.1201/9781315272573, 2006.

https://doi.org/10.5194/egusphere-2024-3580
Preprint. Discussion started: 23 January 2025

Xu, X., Derksen, C., Yueh, S.H., Dunbar, R.S., and Colliander, A.: Freeze/Thaw Detection and Validation Using Aquarius' L-Band Backscattering Data, IEEE Journal of Selected Topics in Applied Earth Observations and Remote Sensing, 9, 1370–1381, doi.10.1109/JSTARS.2016.2519347, 2016

Yi, Y., Kimball, J., Chen, R., Moghaddam, M., and Miller, C.: Sensitivity of active layer freezing process to snow cover in Arctic Alaska, The Cryosphere, 1–39, doi.10.5194/tc-2018-170, 2018.

Zhang, Y., Sherstiukov, A.B., Qian, B., Kokelj, S. v., and Lantz, T.C.: Impacts of snow on soil temperature observed across the circumpolar north, Environmental Research Letters, 13, doi.10.1088/1748-9326/aab1e7 , 2018.

Zheng, D., Wang, X., van der Velde, R., Zeng, Y., Wen, J., Wang, Z., Schwank, M., Ferrazzoli, P., and Su, Z.: L-band microwave emission of soil freeze-thaw process in the third pole environment, IEEE Transactions on Geoscience and Remote Sensing, 55, 5324–5338, doi.10.1109/TGRS.2017.2705248, 2017.